Journal of Zhejiang University-SCIENCE A 2026 27(4):348-364
www.jzus.zju.edu.cn; www.springer.com/journal/11582
E-mail: jzus_a@zju.edu.cn

Research Article
https://doi.org/10.1631/jzus.A2500172

Fixed-time robust attitude tracking control for high-speed aircraft: a precise funnel-guided approach

Kai AN, Wei HUANG✉, Shuangxi LIU

Advanced Propulsion Technology Laboratory, National University of Defense Technology, Changsha 410073, China

Abstract: In this article, we present a fixed-time robust attitude control scheme with severe funnel driving constraints for high-speed aircraft developed concerning uncertain signals. First, an adaptive fixed-time radial basis function neural network (AFTR) observer is described, designed as a compensation control based on a converted attitude error system, aiming at eliminating the influence of strong disturbances and uncertainties. Then, we propose a performance-prescribed transformation strategy that can effectively enhance the accuracy of error tracking and state convergence by constructing second-order performance error functions. Based on the above preparation and transformation, we present a double-integral fixed-time sliding mode controller combined with an auxiliary oscillation-suppression function designed to achieve fixed-time convergence of attitude angles and angular rates, which ensures the rapidity of error tracking and state convergence. Finally, the fixed-time stability of the entire closed-loop system is proved via Lyapunov synthesis theory, and the upbound of convergence time is derived. Nominal and comparative simulation cases were used to investigate the effectiveness and reliability of the proposed integrated framework.

Key words: Funnel control; Fixed-time theory; Attitude control; Radial basis function neural network (RBFNN); High-speed aircraft

1 Introduction

High-performance attitude control has a profound effect on the success of unmanned vehicle missions, such as the learning control of quadruped robots (Wu et al., 2023), the navigation, guidance, and control of unmanned aerial vehicles (Chen et al., 2024), the path tracking of a sailboat (Wu et al., 2023), and the orbiting entry, landing, and sample return of the Chang'e lunar exploration program (Liu et al., 2021). It is crucial for high-speed aircraft systems with complex dynamic coupled characteristics and environmental constraints to have a rapid signal response and anti-disturbance capability. The techniques of performance-prescribed control (PPC), fixed-time control (FTC), and radial basis function neural network (RBFNN) have emerged as prominent research fields.

PPC was originally introduced by Bechlioulis and Rovithakis (2008) with the objective of obtaining predetermined steady-state and transient performance. The effective performance function is the essential feature that differentiates the PPC from other control approaches. Furthermore, the design of the performance function has an immediate impact on the final simulation results. Due to its shape, the performance function is also referred to as the funnel function (Berger and Rauert, 2020). Many performance functions integrated with different control methodologies have been developed for high-speed aircraft. Bu (2023) developed a performance function independent of initial state errors by combining it with an exponential function for longitudinal fuzzy control, which enhances the flexibility of boundary adjustment. A boundary-adjustable prescribed performance controller combined with a backstepping technique was proposed by Wang and Hu (2018) to address the perturbation and saturation issues of a sudden system crash. This was further improved by Bu et al. (2023), Song and Zhang (2024), and Lun et al. (2024) to tolerate sudden error fluctuations. Some scholars have also demonstrated the advantages of PPC by integrating performance functions with control methods such as dynamic surface control (Yin et al., 2024) and output feedback control (Li et al.,

✉ Wei HUANG, gladrain2001@163.com
Wei HUANG, https://orcid.org/0000-0001-9805-985X

Received May 8, 2025; Revision accepted Sept. 16, 2025;
Crosschecked Jan. 14, 2026; Online first Mar. 17, 2026

2023). With the development of intelligent approaches, Xu et al. (2022) extended the finite-time performance function proposed by Tan and Guo (2022) to the attitude control of high-speed aircraft and proposed a fixed-time control scheme based on a reinforcement learning module. Zhao et al. (2023a) developed a hybrid intelligent controller considering prescribed performance constraints and a critic-only adaptive dynamic programming approach. However, these methods have some reliability issues. A typical problem is that the tracking state errors approach boundaries and repeat high-frequency oscillations, which seriously compromises system stability. In addition, a sufficient convergence space (i.e., large steady-state error range) may sacrifice the transition performance and cause unstable transient histories of errors. As a complementary transformation measurement, the PPC scheme needs to be combined with other control methods to realize its performance advantages.

In view of its advantages, fixed-time theory (Polyakov, 2012) can be introduced into the PPC framework to provide accurate system control. Fixed-time convergence establishes stricter theoretical limitations than asymptotic and finite-time control methods. It requires an analytically explicit expression for the upper bound constraint of convergence time, which enables the overall convergence time of the system to be controllable through parameter modification. Fixed-time theory combined with sliding mode control has been widely applied to high-speed aircraft (Parsegov et al., 2012; Zuo and Tie, 2014), and shows that the fixed settling time can be estimated for any initial state. Wu et al. (2021) designed a quantized double-loop fixed-time fault-tolerant attitude controller with a fixed-time extended state observer to ensure overall control performance. Similarly, Dong et al. (2022) developed a fixed-time fuzzy adaptive fault-tolerant control methodology. Chen et al. (2023) designed a double-integral fixed-time sliding mode manifold and fixed-time controller to avoid the decoupling problem of complex attitude variation of high-speed morphing aircraft. Zhang H et al. (2024) further developed a fixed-time flight control strategy based on homogenous system theory. Furthermore, an event-triggered mechanism was introduced into a specific fixed-time control theory proposed by Moulay et al. (2022) to maintain the robustness of the attitude system and reduce the control updating frequency (Zhang et al., 2023). Zhao et al. (2022) designed a fixed-time attitude control scheme combined with the backstepping technique. In addition to integration with conventional control approaches, intelligent learning is increasingly expanding the range of applications for fixed-time theory, such as the finite-time deterministic learning control framework proposed by Guo and Xu (2022), barrier Lyapunov function-based predefined time learning control (Wang et al. 2024), and intelligent fault diagnosis-based fixed-time learning control scheme (Wang and Xia, 2024). Overall, the fixed-time theory has the capability to stabilize state errors rapidly, but there is still an extensive requirement to respond to strong coupled high-speed aircraft systems and further enhance the research exploration of applications.

With the appropriate parameters, PPC and fixed-time theory can effectively drive the tracking errors to arbitrarily small values if the system is not influenced by uncertain signals. However, it is necessary to introduce a compensation observer to estimate the external disturbances and propagated uncertainties within the system, which may make the system diverge (Bouaiss et al., 2024). As an intelligent approximation method, the RBFNN can effectively address the trade-off between function complexity and approximation accuracy through its inherent neural network (NN) capabilities. This method has already been extensively explored in model approximation (Bao et al., 2023), parameter estimation (Shen et al., 2023; Zhang BC et al., 2024), and disturbance prediction (Zhao and Yang, 2022; Zhao et al., 2023b) in high-speed aircraft systems. However, RBF networks generally fail to meet the requirements for convergence speed and are unable to rapidly predict system disturbances based on dynamic responses. The fixed-time control theory emphasizes the guaranteed convergence speed of the system, which ensures that the system can reach a steady-state convergence region within a predefined upper bound of time, expressed in explicit analytical form. This avoids potential instability issues (Sun et al., 2020; Ding et al., 2022), ensuring swift estimation of disturbances. By leveraging the fitting capability of the RBFNN and the fixed-time convergence guaranteed by fixed-time adaptive laws, developing a composite disturbance observer will effectively achieve a feasible trade-off between estimation accuracy and convergence speed. Meng et al. (2024) developed a fixed-time RBFNN disturbance observer and derived a fitting error expression for reusable launch

vehicles. Li et al. (2024) designed a fixed-time disturbance observer for inertia uncertainties in attitude tracking control of spacecraft. Thus, it is imperative to design a secure observer by combining RBFNN with fixed-time theory for potential disturbance. A complete summary of the adaptive updating law design and detailed system analysis for the complicated and coupled angle/angular rate system will be outlined.

Motivated by the above discussion and based on the preceding research foundation of sliding mode control (An et al., 2022), the integrated attitude-tracking control approach was further developed for a generic high-speed model within a disturbed flight environment. The main contributions of this article are as follows:

(1) Faced with the weakness of wide boundaries of steady-state error and uncontrollable error trajectories of existing PPC approaches applied in attitude control (Bu and Xiao, 2018; Wang and Hu, 2018; Bu, 2023; Bu et al., 2023; Li et al., 2023; Lun et al., 2024; Song and Zhang, 2024; Yin et al., 2024), a funnel-guided PPC scheme combined with improved funnel boundaries is proposed to eliminate the unexpected transition history, reach narrow steady-state error thresholds, and achieve rapid error convergence.

(2) Compared with the existing fixed-time sliding mode controllers of Chen et al. (2023), an effective double-integral fixed-time sliding mode manifold is proposed to guarantee stable and rapid convergence of the attitude angles and angular rates. To eliminate asymptotic oscillation in the tracking process, an auxiliary oscillation-suppression function is designed simultaneously, which has been proven to have a good effect.

(3) To address the significant effects of uncertain signals, a fixed-time RBFNN enhancement observer with a developed adaptive weight updating law named AFTR is designed to eliminate unknown disturbances and uncertainties from the dynamic model, atmosphere parameters, and perturbation factors in both attitude angle and angular rate channels.

The rest of this article is organized as follows: Section 2 introduces the approach with some preliminary notes and lemmas, and describes the problem formulation. Section 3 provides the main results, including the AFTR enhancement observer, funnel-guided PPC, fixed-time sliding mode tracking controller, and parameter tuning guideline, together with corresponding demonstrations of stability. Finally, numerical simulations are presented in Section 4.

2 Preliminaries and problem formulation

2.1 Preliminaries

Lemma 1 (Chen et al., 2021) Assume there is a continuous positive definite and radially unbounded function $\mathcal{V}(x)$ with state x such that $\dot{\mathcal{V}}(x)\leqslant-\mathcal{K}_1\mathcal{V}^{p_1}(x)-\mathcal{K}_2\mathcal{V}^{q_1}(x)+\xi$, where $\mathcal{K}_1$, $\mathcal{K}_2>0$, satisfying $0<p_1<1$, $q_1>1$, and ξ denotes a small positive constant. The system will converge to the origin x_0 in fixed-time equilibrium with settling time $\mathcal{T}_1(x_0)$ bounded by

$$\mathcal{T}_1(x_0)\leqslant\mathcal{T}_{1,\max}=\frac{1}{\mathcal{K}_1\delta(1-p_1)}+\frac{1}{\mathcal{K}_2\delta(q_1-1)}.$$

The residual set Q of the system is given as follows, with constant $0<\delta<1$, where $\min\{\cdot\}$ represents the minimum value:

$$Q=\left\{x\left|\mathcal{V}(x)\leqslant\min\left\{\left[\frac{\xi}{\mathcal{K}_1(1-\delta)}\right]^{\frac{1}{p_1}},\left[\frac{\xi}{\mathcal{K}_2(1-\delta)}\right]^{\frac{1}{q_1}}\right\}\right.\right\}.$$

Lemma 2 (Xin et al., 2023) According to Corollary 1 of Xin et al. (2023), for a continuous Lyapunov function like $\dot{\mathcal{V}}(x)\leqslant-\mathcal{K}_1\mathcal{V}^{\frac{q_1}{q_2}}(x)-\mathcal{K}_2\mathcal{V}^{\frac{q_1}{q_2}}(x)-\mathcal{K}_3\mathcal{V}(x)+\epsilon$, where $\mathcal{K}_1$, $\mathcal{K}_2$, $\mathcal{K}_3>0$, $0<\epsilon<\infty$, then the system $\dot{x}=f(x,t)$, $x(0)=0$ is semiglobal practical fixed-time stability (SPFS), in which the fixed convergence time $\mathcal{T}_2$ is given by

$$\mathcal{T}_2\leqslant\mathcal{T}_{2,\max}=\max\left\{\frac{\alpha_2\ln\left(1+\frac{\mathcal{K}_3}{\delta\mathcal{K}_1}\right)}{\mathcal{K}_3(\alpha_1-\alpha_2)},\frac{\alpha_2\ln\left(1+\frac{\delta\mathcal{K}_3}{\mathcal{K}_1}\right)}{\delta\mathcal{K}_3(\alpha_1-\alpha_2)}\right\}+\max\left\{\frac{\beta_2\ln\left(1+\frac{\mathcal{K}_3}{\delta\mathcal{K}_2}\right)}{\mathcal{K}_3(\beta_2-\beta_1)},\frac{\beta_2\ln\left(1+\frac{\delta\mathcal{K}_3}{\mathcal{K}_2}\right)}{\delta\mathcal{K}_3(\beta_2-\beta_1)}\right\},$$

where α_1, α_2, β_1, and β_2 are all positive odd numbers and $\alpha_1>\alpha_2$, $\beta_1<\beta_2$, $\max\{\cdot\}$ represents the maximum value, $0<\delta<1$, and the residual set Q with output $\mathcal{Y}(x)$ of the system is expressed as

$$Q=\left\{x\left|\mathcal{Y}(x)\leqslant\min\left\{\left[\frac{\epsilon}{\mathcal{K}_1(1-\delta)}\right]^{\frac{\alpha_2}{\alpha_1}},\left[\frac{\epsilon}{\mathcal{K}_2(1-\delta)}\right]^{\frac{\beta_2}{\beta_1}},\frac{\epsilon}{\mathcal{K}_3(1-\delta)}\right\}\right.\right\}.$$

Lemma 3 (Zuo, 2015) For $x_i \in \mathbb{R}^+ (i=1, 2, \cdots, n)$:

$$\sum_{i=1}^{n} |x_i|^{\chi} \geqslant \begin{cases} \left(\sum_{i=1}^{n} |x_i| \right)^{\chi}, & 0<\chi \leqslant 1, \\ n^{1-\chi} \left(\sum_{i=1}^{n} |x_i| \right)^{\chi}, & \chi>1. \end{cases}$$

Lemma 4 (Qian and Lin, 2001) For the constants $\mathcal{K}_1>1$ and $\mathcal{K}_2>1$, if the equation $\frac{1}{\mathcal{K}_1} + \frac{1}{\mathcal{K}_2} = 1$ holds, then the following expression is established:

$$|xy| \leqslant \frac{\epsilon^{\mathcal{K}_1}}{\mathcal{K}_1} |x|^{\mathcal{K}_1} + \frac{1}{\mathcal{K}_2 \epsilon^{\mathcal{K}_2}} |y|^{\mathcal{K}_2},$$

for arbitrary $x \in \mathbb{R}$, $y \in \mathbb{R}$, and $\epsilon>0$.

2.2 Dynamics modeling and problem description

The differential attitude subsystem with angle of attack α, sideslip angle β, and bank angle μ as tracking states is as follows:

$$\begin{cases} \dot{\alpha} = q - \tan\beta (p\cos\alpha + r\sin\alpha) + \dfrac{-L + \overline{G}_{\alpha} + \overline{F}_{\mathrm{d}\alpha}}{m_0 V \cos\beta}, \\ \dot{\beta} = p\sin\alpha - r\cos\alpha + \dfrac{Y + \overline{G}_{\beta} + \overline{F}_{\mathrm{d}\beta}}{m_0 V}, \\ \dot{\mu} = \dfrac{p\cos\alpha + r\sin\alpha}{\cos\beta} + \dfrac{\overline{G}_{\mu} + \overline{F}_{\mathrm{d}\mu}}{m_0 V} + \\ \qquad \dfrac{L(\tan\beta + \tan\gamma\sin\mu) + Y\tan\gamma\cos\mu}{m_0 V}, \end{cases} \tag{1}$$

where q, r, and p represent the angular rates of pitch, yaw, and roll, respectively, m_0 is the mass, V is the velocity, L is the lift force, Y is the side force, and γ is the flight path angle. $\overline{\boldsymbol{F}}_{\mathrm{d}} = [\overline{F}_{\mathrm{d}\alpha}, \overline{F}_{\mathrm{d}\beta}, \overline{F}_{\mathrm{d}\mu}]^{\mathrm{T}}$ are the aerodynamic disturbance force components acting on the three channels. $\overline{\boldsymbol{G}} = [\overline{G}_{\alpha}, \overline{G}_{\beta}, \overline{G}_{\mu}]^{\mathrm{T}}$ represents the equivalent components of gravity in the three control channels. The detailed expression of $\overline{\boldsymbol{G}}$ is given in Eq. (S1) of the electronic supplementary materials (ESM).

The angular rate subsystem is described as

$$\begin{cases} \dot{q} = \dfrac{J_x - J_x}{J_y} pr + \dfrac{M_m + x_{\mathrm{cg}}(D\sin\alpha + L\cos\alpha) + \Delta M_Y}{J_y}, \\ \dot{r} = \dfrac{J_x - J_y}{J_z} pq + \dfrac{M_n - x_{\mathrm{cg}} Y + \Delta M_Z}{J_z}, \\ \dot{p} = \dfrac{J_y - J_z}{J_x} qr + \dfrac{M_l + \Delta M_X}{J_x}, \end{cases} \tag{2}$$

where the lift force L, drag force D, and side force Y can be written as $L=C_L \bar{q} S$, $D=C_D \bar{q} S$, and $Y=C_Y \bar{q} S$, and the force moments for the three axes are $M_l = C_l \bar{q} b S$, $M_m = C_m \bar{q} c S$, and $M_n = C_n \bar{q} b S$. C_L, C_D, C_Y, C_l, C_m, and C_n are the aerodynamic coefficients (Keshmiri et al., 2012). b is the wingspan, and c is the mean aerodynamic chord. The dynamic pressure is calculated by $\bar{q} = \frac{1}{2} \bar{\rho} V^2$ with atmospheric density $\bar{\rho}$. S is the surface area of the vehicle, x_{cg} is the center of gravity, and the uncertain moment vector is expressed by $\Delta \boldsymbol{M} = [\Delta M_Y, \Delta M_Z, \Delta M_X]^{\mathrm{T}}$. $\boldsymbol{J} = \mathrm{diag}\{J_y, J_z, J_x\}$ represents the moment of inertia.

The above two subsystems can be simplified as a general nonlinear vector expression:

$$\begin{aligned} \dot{\boldsymbol{\Omega}} &= \boldsymbol{g}_{\boldsymbol{\Omega}} \boldsymbol{\omega} + \boldsymbol{\Delta}_{\boldsymbol{\Omega}}, \\ \dot{\boldsymbol{\omega}} &= \boldsymbol{f}_{\boldsymbol{\omega}} + (\boldsymbol{g}_{\boldsymbol{\omega}} + \Delta \boldsymbol{g}_{\boldsymbol{\omega}}) \boldsymbol{u} + \boldsymbol{\Delta}_{\boldsymbol{\omega f}}, \end{aligned} \tag{3}$$

where $\boldsymbol{\Omega} = [\alpha, \beta, \mu]^{\mathrm{T}}$, $\boldsymbol{\omega} = [q, r, p]^{\mathrm{T}}$, and $\boldsymbol{u} = [\delta_{\mathrm{e}}, \delta_{\mathrm{a}}, \delta_{\mathrm{r}}]^{\mathrm{T}}$ being the control input. The terms $\boldsymbol{\Delta}_{\boldsymbol{\Omega}} = \frac{1}{m_0 V} \left[\frac{\overline{F}_{\mathrm{d}\alpha}}{\cos\beta}, \overline{F}_{\mathrm{d}\beta}, \overline{F}_{\mathrm{d}\mu} \right]^{\mathrm{T}}$ and $\boldsymbol{\Delta}_{\boldsymbol{\omega f}} = \left[\frac{\Delta M_Y}{J_y}, \frac{\Delta M_Z}{J_z}, \frac{\Delta M_X}{J_x} \right]^{\mathrm{T}}$ are caused by unknown disturbances and uncertain components. $\Delta \boldsymbol{g}_{\boldsymbol{\omega}}$ represents the model uncertainties due to aerodynamic perturbation and atmospheric error. The specific expressions for some notations in Eq. (3) are given in Eqs. (S2) and (S3) of the ESM. Let $\boldsymbol{f}_{\boldsymbol{\omega}} = [f_q, f_r, f_p]^{\mathrm{T}}$, and the detailed expressions are given in Eq. (S4) of the ESM.

The angle reference command is denoted as $\boldsymbol{\Omega}_{\mathrm{d}}(t_0)$ in the initial time t_0. To ensure the smooth continuity of the reference signals and protect the control quantity from excessive sudden changes and fluctuations, a first-order filter is introduced into the signal interface. Then, the filtered input signal in the next discretized time point t_1 is obtained by

$$\overline{\boldsymbol{\Omega}}_{\mathrm{d}}(t_1) = k_{\mathrm{ft}} \boldsymbol{\Omega}_{\mathrm{d}}(t_0) + (1 - k_{\mathrm{ft}}) \overline{\boldsymbol{\Omega}}_{\mathrm{d}}(t_0), \tag{4}$$

where k_{ft} is the filter coefficient, and $\overline{\boldsymbol{\Omega}}_{\mathrm{d}}$ is the filtered guidance command.

The following control-oriented second-order error dynamic model Eq. (5) is then developed as follows, based on the attitude model of Eq. (3). This model aims to convert the original state errors to assist the

construction of subsequent dual-channel fixed-time controllers.

$$\begin{aligned}\dot{\boldsymbol{e}}_{\Omega}&=\dot{\boldsymbol{\Omega}}-\dot{\bar{\boldsymbol{\Omega}}}_{\mathrm{d}}=\boldsymbol{g}_{\Omega}\boldsymbol{\omega}-\dot{\bar{\boldsymbol{\Omega}}}_{\mathrm{d}}+\boldsymbol{\Delta}_{\Omega},\\ \dot{\boldsymbol{e}}_{\omega}&=\dot{\boldsymbol{\omega}}-\dot{\boldsymbol{\omega}}_{\mathrm{d}}=\boldsymbol{f}_{\omega}+\boldsymbol{g}_{\omega}\boldsymbol{u}-\dot{\boldsymbol{\omega}}_{\mathrm{d}}+\boldsymbol{\Delta}_{\omega},\end{aligned}\tag{5}$$

where $\boldsymbol{\omega}_{\mathrm{d}}$ represents the reference angular rate, which can be obtained by the angular subsystem through the backstepping method, and $\boldsymbol{\Delta}_{\omega}=\Delta\boldsymbol{g}_{\omega}\boldsymbol{u}+\boldsymbol{\Delta}_{\omega f}$.

Based on the above dynamic models and relevant parameters, the main purpose of this study was to develop a funnel-guided fixed-time controller (FGFTC) with an AFTR observer to address the following issues:

1. Estimate the unknown comprehensive uncertainties $\boldsymbol{\Delta}_{\Omega}$ and $\boldsymbol{\Delta}_{\omega}$ composed of aerodynamic perturbation, external disturbances, and atmospheric uncertainties precisely, and then derive the fixed-time convergence characteristics with the designed AFTR observer.

2. With the given initial state conditions and guided performance-prescribed funnel, the attitude angle error vector $\boldsymbol{e}_{\Omega}$ and the angular rate error vector $\boldsymbol{e}_{\omega}$ can achieve fast convergence to the equilibrium points of the control system in fixed time.

3 Results

First, we introduce an observer design to address inherent uncertainties in nonlinear systems (Eq. (3)) and external disturbances. Then, a fixed-time robust controller for an attitude closed-loop system is presented, featuring a performance-prescribed funnel shrinking guidance for transforming error dynamics. Meanwhile, an auxiliary oscillation-suppressing measure is implemented in the proposed controller to facilitate rapid oscillation elimination. The integrated fixed-time control framework developed in this study is illustrated in Fig. 1, and the detailed design procedure is provided below.

3.1 AFTR enhancement observer

Considering the nonlinear system of Eq. (3), define error vectors $\boldsymbol{z}_{\Omega}=\boldsymbol{\Omega}-\bar{\boldsymbol{\Omega}}_{\mathrm{d}}$, $\boldsymbol{z}_{\omega}=\boldsymbol{g}_{\Omega}\boldsymbol{\omega}-\dot{\bar{\boldsymbol{\Omega}}}_{\mathrm{d}}$, and then the system can be rewritten as

$$\begin{aligned}\dot{\boldsymbol{z}}_{\Omega}&=\boldsymbol{z}_{\omega}+\boldsymbol{\Delta}_{\Omega},\\ \dot{\boldsymbol{z}}_{\omega}&=\boldsymbol{F}_{\omega}+\boldsymbol{G}_{\omega}\boldsymbol{u}+\boldsymbol{\Delta}_{\omega},\end{aligned}\tag{6}$$

where $\boldsymbol{F}_{\omega}=\dot{\boldsymbol{g}}_{\Omega}\boldsymbol{\omega}+\boldsymbol{g}_{\Omega}\boldsymbol{f}_{\omega}-\ddot{\bar{\boldsymbol{\Omega}}}_{\mathrm{d}}$, $\boldsymbol{G}_{\omega}=\boldsymbol{g}_{\Omega}\boldsymbol{g}_{\omega}$, and $\boldsymbol{\Delta}_{\omega}=\boldsymbol{g}_{\Omega}(\Delta\boldsymbol{g}_{\omega}\boldsymbol{u}+\boldsymbol{\Delta}_{\omega f})$. The term $\dot{\bar{\boldsymbol{\Omega}}}_{\mathrm{d}}$ can be easily obtained under the assumption that the reference signal is second-order differentiable.

Define a combined vector $\mathcal{Z}=[\boldsymbol{z}_{\Omega}^{\mathrm{T}},\ \boldsymbol{z}_{\omega}^{\mathrm{T}}]^{\mathrm{T}}$, and then the second-order nonlinear system Eq. (6) is rewritten as the compound form:

$$\dot{\mathcal{Z}}=\boldsymbol{A}\mathcal{Z}+\boldsymbol{B}(\boldsymbol{F}_{\omega}+\boldsymbol{G}_{\omega}\boldsymbol{u})+\Delta\mathcal{Z},\tag{7}$$

where $\boldsymbol{A}=\begin{bmatrix}\boldsymbol{0}_{3\times3} & \boldsymbol{1}_{3\times3}\\ \boldsymbol{0}_{3\times3} & \boldsymbol{0}_{3\times3}\end{bmatrix}$, $\boldsymbol{B}=[\boldsymbol{0}_{1\times3},\boldsymbol{1}_{1\times3}]^{\mathrm{T}}$, $\Delta\mathcal{Z}=[\boldsymbol{\Delta}_{\Omega}^{\mathrm{T}},\boldsymbol{\Delta}_{\omega}^{\mathrm{T}}]^{\mathrm{T}}$, $\boldsymbol{0}$ represents a vector with all zeros, and $\boldsymbol{1}$ denotes the vector of all ones.

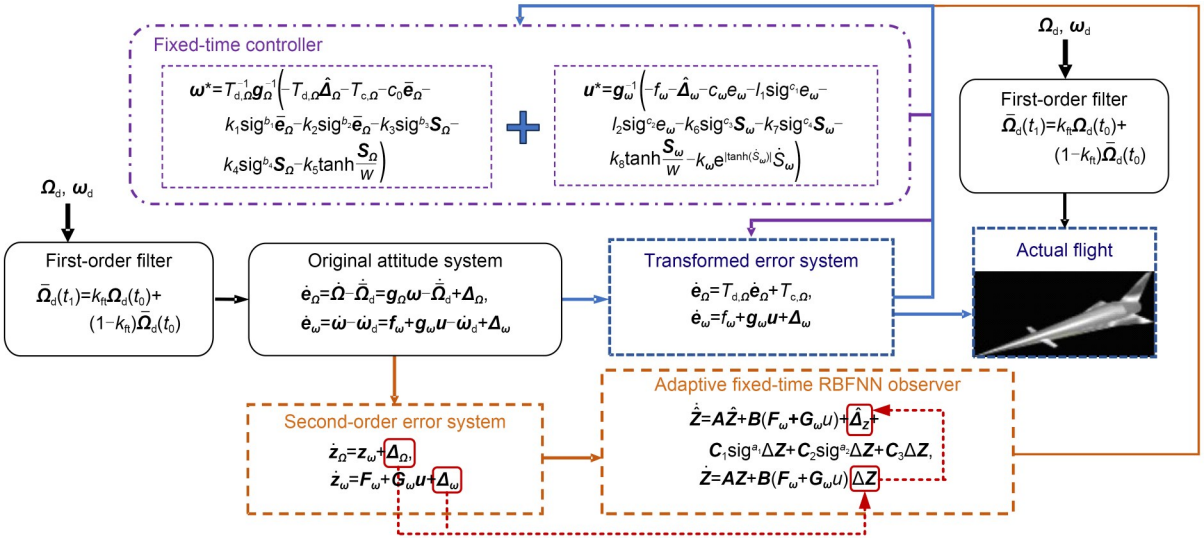

Fig. 1 Integrated fixed-time control framework. The parameters are explained in the text

Before the detailed observer error analysis, the designed AFTR observer is first given as

$$\begin{aligned}\dot{\hat{\boldsymbol{\mathcal{Z}}}}=&\boldsymbol{A}\hat{\boldsymbol{\mathcal{Z}}}+\boldsymbol{B}(\boldsymbol{F}_{\omega}+\boldsymbol{G}_{\omega}\boldsymbol{u})+\hat{\boldsymbol{\Delta}}_{\mathcal{Z}}+\\&\boldsymbol{C}_1\mathrm{sig}^{a_1}\Delta\boldsymbol{\mathcal{Z}}+\boldsymbol{C}_2\mathrm{sig}^{a_2}\Delta\boldsymbol{\mathcal{Z}}+\boldsymbol{C}_3\Delta\boldsymbol{\mathcal{Z}},\end{aligned}\tag{8}$$

where $\boldsymbol{C}_1$ and $\boldsymbol{C}_2$ are both diagonal matrices and the diagonal elements $c_{1,i}$, $c_{2,i}>0$, $\boldsymbol{C}_3=\begin{bmatrix}\boldsymbol{0}_{3\times3} & \boldsymbol{D}_{3\times3}\\ \boldsymbol{0}_{3\times3} & \boldsymbol{0}_{3\times3}\end{bmatrix}$, where $\boldsymbol{D}_{3\times3}=\mathrm{diag}\{d_n\}$, n=1, 2, 3, $d_n>1$. The function $\mathrm{sig}^l\boldsymbol{x}=\mathrm{sgn}(\boldsymbol{x})\|\boldsymbol{x}\|^l$ and $\mathrm{sgn}(\boldsymbol{x})$ represents the sign of $\boldsymbol{x}$. $\hat{\boldsymbol{\mathcal{Z}}}$ is the observed state vector and $\hat{\boldsymbol{\Delta}}_{\mathcal{Z}}$ is the estimated value of comprehensive disturbances and uncertainties for $\hat{\boldsymbol{\mathcal{Z}}}$. $\Delta\boldsymbol{\mathcal{Z}}=\boldsymbol{\mathcal{Z}}-\hat{\boldsymbol{\mathcal{Z}}}$ denotes the observation error, and $a_1\in(0, 1)$, $a_2=2-a_1$. Based on the discussion, the term $\hat{\boldsymbol{\Delta}}_{\mathcal{Z}}$ is approximated by the RBFNN.

Based on the general NN expression from Eqs. (S5) and (S6) of the ESM, the real and estimated disturbance terms $\boldsymbol{\Delta}_{\mathcal{Z}}$ and $\hat{\boldsymbol{\Delta}}_{\mathcal{Z}}$ can be similarly defined by

$$\begin{aligned}\boldsymbol{\Delta}_{\mathcal{Z}}&=\boldsymbol{W}^{\mathrm{T}}\boldsymbol{h}(\boldsymbol{\mathcal{Z}})+\boldsymbol{\epsilon}(\boldsymbol{\mathcal{Z}}),\\ \hat{\boldsymbol{\Delta}}_{\mathcal{Z}}&=\hat{\boldsymbol{W}}^{\mathrm{T}}\boldsymbol{h}(\boldsymbol{\mathcal{Z}}),\end{aligned}\tag{9}$$

where $\boldsymbol{\epsilon}(\boldsymbol{\mathcal{Z}})$ is the NN approximation error, $\boldsymbol{h}(\boldsymbol{\mathcal{Z}})$ is the Gaussian basis function, $\boldsymbol{W}$ and $\hat{\boldsymbol{W}}\in\mathbb{R}^{N\times6}$ are the optimal and approximated weight vectors, respectively, and the corresponding estimated weight errors can be given by

$$\tilde{\boldsymbol{W}}=\boldsymbol{W}-\hat{\boldsymbol{W}}.\tag{10}$$

Assumption 1 (Chen et al., 2023) The NN approximation error $\boldsymbol{\epsilon}(\cdot)$ has an upper bound ϵ_N satisfying $\|\boldsymbol{\epsilon}(\cdot)\|\leqslant\epsilon_N$, and the ideal weights are assumed to be bounded as $\|\boldsymbol{W}\|\leqslant W_N$.

Subscribing Eqs. (7) and (8) into $\Delta\boldsymbol{\mathcal{Z}}$, the following dynamics can be derived:

$$\begin{aligned}\Delta\dot{\boldsymbol{\mathcal{Z}}}=&\boldsymbol{A}\Delta\boldsymbol{\mathcal{Z}}+\tilde{\boldsymbol{W}}^{\mathrm{T}}\boldsymbol{h}(\boldsymbol{\mathcal{Z}})+\boldsymbol{\epsilon}(\boldsymbol{\mathcal{Z}})-\\&\boldsymbol{C}_1\mathrm{sig}^{a_1}\Delta\boldsymbol{\mathcal{Z}}-\boldsymbol{C}_2\mathrm{sig}^{a_2}\Delta\boldsymbol{\mathcal{Z}}-\boldsymbol{C}_3\Delta\boldsymbol{\mathcal{Z}}.\end{aligned}\tag{11}$$

Then, the following convergence theorem of the observer is described and proven.

Theorem 1 The proposed AFTR adaptive enhancement observer (Eq. (8)) can guarantee that the observation error (Eq. (11)) converges to a neighborhood of origin in a fixed time with the NN adaptive weight updating law $\dot{\hat{\boldsymbol{W}}}=\boldsymbol{P}\boldsymbol{h}\Delta\boldsymbol{\mathcal{Z}}^{\mathrm{T}}-\hat{\boldsymbol{W}}$, where $\boldsymbol{P}$ is the constant coefficient matrix. The detailed proof process can be found in Section S2 of the ESM.

Remark 1 Theorem 1 shows that the condition $\|\tilde{\boldsymbol{W}}\|\approx0$ can be satisfied when the system time satisfies $T_s>T_{0,\max}$, meaning that the observation error $\tilde{\boldsymbol{\Delta}}_{\mathcal{Z}}$ will converge to zero in the fixed time T_s with Assumption 1. Thus, it is reasonable to assume that the state errors $\tilde{\boldsymbol{\Delta}}_{\boldsymbol{\Omega}}$ and $\tilde{\boldsymbol{\Delta}}_{\omega}$ have upper bounds satisfying $\|\tilde{\boldsymbol{\Delta}}_{\boldsymbol{\Omega}}\|\leqslant D_{\boldsymbol{\Omega}}$ and $\|\tilde{\boldsymbol{\Delta}}_{\omega}\|\leqslant D_{\omega}$ when the convergence time $T_0>T_s$. Meanwhile, it can be further assumed that the derivatives $\dot{\tilde{\boldsymbol{\Delta}}}_{\boldsymbol{\Omega}}$ and $\dot{\tilde{\boldsymbol{\Delta}}}_{\omega}$ exist and are continuously bounded, satisfying $\left\|\dot{\tilde{\boldsymbol{\Delta}}}_{\boldsymbol{\Omega}}\right\|\leqslant D_{\boldsymbol{\Omega}}$ and $\left\|\dot{\tilde{\boldsymbol{\Delta}}}_{\omega}\right\|\leqslant D_{\omega}$.

3.2 Funnel-guided prescribed performance methodology

In general, the metrics of control performance are expressed by steady-state error, transition history, and settling time. Unrestricted states may lead to uncontrollable transitional convergence histories and invalid control signals over a prolonged period. The performance-prescribed technique sets strict boundaries for error states during the entire convergence phase, ensuring that tracking errors can remain within certain intervals to meet performance requirements.

The tracking errors of angle states expressed by Eq. (5) are constrained by the designed boundaries named funnel functions, which can be introduced by $-\rho_{\mathcal{L}}(t)\leqslant e_i(t)\leqslant\rho_{\mathcal{U}}(t)$, $i=\alpha, \beta, \mu$, where $\rho_{\mathcal{L}}(t)$ and $\rho_{\mathcal{U}}(t)$ are the lowbound and upbound functions. The smooth funnel functions $\rho_{\mathcal{L}}(t)$ and $\rho_{\mathcal{U}}(t)$ must satisfy two requirements: (1) $\rho_{\mathcal{L}}(t)$, $\rho_{\mathcal{U}}(t)>0$ are continuously differentiable functions, and $\lim_{t\to\infty}\rho_j(t)=\rho_{j,\infty}$, $j=\mathcal{L}$, $\mathcal{U}$, and $\rho_{j,\infty}$ is the steady-state error boundary; (2) the derivative of the funnel function is semi-negative definite. The traditional exponential funnel function of Bechlioulis and Rovithakis (2008) and some improved funnel functions (Bu and Xiao, 2018; Wang and Hu, 2018; Bu, 2023; Bu et al., 2023; Li et al., 2023; Lun et al., 2024; Song and Zhang, 2024; Yin et al., 2024) still show some conflicts in terms of generality while being effectively applied to solve their relevant scientific challenges: 1° wide steady-state error boundaries; 2° uncontrollable error trajectories. This section is focused mainly on shrinking the steady-state error range and accelerating the convergence of error trajectories.

Taking the challenge term 1° into account, we present an improved funnel function that has stable transition performance and adjustable steady-state error boundaries. The proposed funnel function is defined as follows:

$$\begin{aligned}&\rho(t)=\rho_0/\cosh(lt),\\ &\rho_{\mathcal{L}}(t)=-\operatorname{sgn}(e_i(0))\tanh\left(\frac{e_i(0)}{a_\rho}\right)\rho(t)-\rho_{i,\infty},\\ &\rho_{\mathcal{U}}(t)=\operatorname{sgn}(e_i(0))\tanh\left(\frac{e_i(0)}{a_\rho}\right)\rho(t)+\rho_{i,\infty},\end{aligned}\tag{12}$$

where ρ_0 is the initial boundary, l is a constant determining the convergence speed of the performance-prescribed boundary, $e_i(0)$ is the initial error of state i, $\rho_{i,\infty}$ denotes the ultimate steady-state error of state i, and a_ρ is a constant satisfying $a_\rho\in(0, 1)$. Because of the properties of the hyperbolic tangent function, a_ρ should be appropriately provided in the simulation for an effective steady-state error history range.

Remark 2 The hyperbolic tangent function, denoted as tanh(·), serves as an adaptive variable constraint term to limit the initial error. This function has two main features: (1) it can indirectly indicate the positivity or negativity of the original state error; (2) it can adaptively enlarge or reduce the constraint boundaries. Finally, the tracking errors will converge to predefined steady-state values with gradually shrinking performance limitations.

Considering the second challenge 2°, a funnel-guided error transition strategy is proposed to lead to the error convergence trajectory. Define an auxiliary variable $s_{i,e}=e_i-e_{i,\mathrm{op}}$, $i=\alpha, \beta, \mu$, $e_{i,\mathrm{op}}=k_{\mathrm{s}}\rho_{\mathcal{L}}+(1-k_{\mathrm{s}})\rho_{\mathcal{U}}$ and $k_{\mathrm{s}}\in(0, 1)$, and then the derivative of $s_{i,e}$ is given by $\dot{s}_{i,e}=\dot{e}_i-\dot{e}_{i,\mathrm{op}}$. Then, the range of $s_{i,e}$ is simultaneously transformed into $s_{\mathcal{L}}(t)\leqslant s_{i,e}(t)\leqslant s_{\mathcal{U}}(t)$, $s_{\mathcal{L}}(t)=\rho_{\mathcal{L}}(t)-e_{i,\mathrm{op}}$ and $s_{\mathcal{U}}(t)=\rho_{\mathcal{U}}(t)-e_{i,\mathrm{op}}$.

To convert the auxiliary error variable into the unconstrained space, the following transformation function is defined:

$$\begin{aligned}&\bar{e}(t)=\ln\left(\frac{\zeta(t)}{1-\zeta(t)}\right),\\ &\zeta(t)=\frac{s_{i,e}(t)-s_{\mathcal{L}}(t)}{s_{\mathcal{U}}(t)-s_{\mathcal{L}}(t)}.\end{aligned}\tag{13}$$

Then, the transformed error equation can be derived by Eq. (14), where the terms T_{d} and T_{c} are described in Eq. (S14) of the ESM.

$$\begin{aligned}\dot{\bar{e}}(t)=&\frac{\dot{\zeta}(t)}{\zeta(t)}\left(1+\frac{\zeta(t)}{1-\zeta(t)}\right)=\frac{s_{\mathcal{U}}-s_{\mathcal{L}}}{(s_{i,e}-s_{\mathcal{L}})(s_{\mathcal{U}}-s_{i,e})}\dot{s}_{i,e}+\\ &\frac{s_{i,e}(\dot{s}_{\mathcal{L}}-\dot{s}_{\mathcal{U}})-\dot{s}_{\mathcal{L}}s_{\mathcal{U}}+\dot{s}_{\mathcal{U}}s_{\mathcal{L}}}{(s_{i,e}-s_{\mathcal{L}})(s_{\mathcal{U}}-s_{i,e})}=T_{\mathrm{d}}\dot{s}_{i,e}+T_{\mathrm{c}}.\end{aligned}\tag{14}$$

Remark 3 Note that if $s_{i,e}\to 0$, the state error e_i will converge to $e_{i,\mathrm{op}}$. The coefficient k_{s} is crucial to control the error convergence trajectories, which will influence the transient performance of e_i and significantly enhance the controllability and stability during the error convergence process. Based on the above discussion, the performance-prescribed transformation method in this article is called the funnel-guided convergence strategy.

Remark 4 Some singularity issues will occur in Eq. (13). This is manifested mainly in the following aspects: First, the large convergence speed with the small steady-state boundary of the funnel boundary is infeasible. In this case, the controller in the angular velocity loop cannot respond rapidly to changes in the reference angular rate, resulting in the accumulation of angle errors and causing the error value to exceed the funnel boundary. Second, an improper value of k_{s} will lead to a significant discrepancy between the actual initial angle error and the reference value. In this case, the controller in the angular velocity loop will deviate from the reference angular rate command during the initial period, resulting in the accumulation of angle errors and causing the error value to exceed the funnel boundary. Therefore, it is necessary to coordinate the relationship between the funnel boundary convergence speed, the steady-state error boundary, the reference error trajectory, and the dynamic characteristics of the angular rate loop based on the parameter tuning guideline in Section 3.5 to effectively avoid singularity issues in Eq. (13).

Based on the designed funnel function Eq. (12) and transformed guidance strategy Eq. (14), the error dynamics of the attitude angle loop in Eq. (5) is further rewritten as the following expression, and the angular rate loop holds:

$$\begin{aligned}&\dot{\boldsymbol{e}}_{\boldsymbol{\Omega}}=\boldsymbol{T}_{\mathrm{d},\boldsymbol{\Omega}}\dot{\boldsymbol{e}}_{\boldsymbol{\Omega}}+\boldsymbol{T}_{\mathrm{c},\boldsymbol{\Omega}},\\ &\dot{\boldsymbol{e}}_{\boldsymbol{\omega}}=\boldsymbol{f}_{\boldsymbol{\omega}}-\dot{\boldsymbol{\omega}}_{\mathrm{d}}+\boldsymbol{g}_{\boldsymbol{\omega}}\boldsymbol{u}+\boldsymbol{\Delta}_{\boldsymbol{\omega}},\end{aligned}\tag{15}$$

where $\boldsymbol{T}_{\mathrm{d},\boldsymbol{\Omega}}$ and $\boldsymbol{T}_{\mathrm{c},\boldsymbol{\Omega}}$ are described in Eq. (S15) of the ESM.

Remark 5 In this article, only the angle states are transformed into the performance-prescribed constraints, and the angular rates will maintain convergence characteristics by the following fixed-time angular controller for two reasons. First, the stable angle error trajectories can provide high-quality input signals for angular rates to minimize the divergence risk, and second, the strict-limitation angular rates will complicate parameter tuning and system structure, which may worsen the controller oscillation frequency and is not practical for real-world applications.

3.3 Fixed-time attitude tracking controller design

Based on the proposed AFTR and performance-prescribed methodology, a fixed-time attitude tracking control scheme was developed to ensure strong stability of the entire closed-loop flight control system.

For the attitude angle control subsystem, considering the transformed state error $\bar{\boldsymbol{e}}_{\boldsymbol{\Omega}}=[\bar{e}_{\alpha},\ \bar{e}_{\beta},\ \bar{e}_{\mu}]^{\mathrm{T}}\in\mathbb{R}^3$, the double-integral sliding mode manifold $\boldsymbol{S}_{\boldsymbol{\Omega}}$ is constructed by

$$\boldsymbol{S}_{\boldsymbol{\Omega}}=\bar{\boldsymbol{e}}_{\boldsymbol{\Omega}}+c_0\int_0^t\bar{\boldsymbol{e}}_{\boldsymbol{\Omega}}\,\mathrm{d}\tau+\int_0^t k_1\,\mathrm{sig}^{b_1}\bar{\boldsymbol{e}}_{\boldsymbol{\Omega}}+k_2\mathrm{sig}^{b_2}\bar{\boldsymbol{e}}_{\boldsymbol{\Omega}}\mathrm{d}\tau, \quad (16)$$

where c_0, k_1, k_2, b_1, and b_2 are all constants, and $b_1>1$, $0<b_2<1$.

A desired virtual angular rate controller $\boldsymbol{\omega}^*$ can be designed as

$$\begin{aligned}\boldsymbol{\omega}^*=T_{\mathrm{d},\boldsymbol{\Omega}}^{-1}\boldsymbol{g}_{\boldsymbol{\Omega}}^{-1}\Big(&-T_{\mathrm{d},\boldsymbol{\Omega}}\hat{\boldsymbol{\Delta}}_{\boldsymbol{\Omega}}-T_{\mathrm{c},\boldsymbol{\Omega}}-c_0\bar{\boldsymbol{e}}_{\boldsymbol{\Omega}}-\\&k_1\mathrm{sig}^{b_1}\bar{\boldsymbol{e}}_{\boldsymbol{\Omega}}-k_2\mathrm{sig}^{b_2}\bar{\boldsymbol{e}}_{\boldsymbol{\Omega}}-k_3\mathrm{sig}^{b_3}\boldsymbol{S}_{\boldsymbol{\Omega}}-\\&k_4\mathrm{sig}^{b_4}\boldsymbol{S}_{\boldsymbol{\Omega}}-k_5\tanh\frac{\boldsymbol{S}_{\boldsymbol{\Omega}}}{w}\Big),\end{aligned} \quad (17)$$

where k_3, k_4, $k_5>0$, $b_3>1$, $0<b_4<1$, and $w>0$.

The two integral terms of the proposed sliding mode manifold $\boldsymbol{S}_{\boldsymbol{\Omega}}$ can ensure that the output can closely match a small steady-state error. However, such a treatment may destabilize and slow down the dynamic response of a closed-loop system. Further simulation tests reveal that ensuring the dynamic response at the convergence stage by tuning parameters alone is challenging. Therefore, to improve the dynamic transition characteristics of the system, an ancillary control term $\boldsymbol{u}_{\mathrm{comp}}$ is designed to compensate the controller Eq. (17) as follows:

$$\begin{aligned}\boldsymbol{\omega}^*=T_{\mathrm{d},\boldsymbol{\Omega}}^{-1}\boldsymbol{g}_{\boldsymbol{\Omega}}^{-1}\Big(&-T_{\mathrm{d},\boldsymbol{\Omega}}\hat{\boldsymbol{\Delta}}_{\boldsymbol{\Omega}}-T_{\mathrm{c},\boldsymbol{\Omega}}-c_0\bar{\boldsymbol{e}}_{\boldsymbol{\Omega}}-\\&k_1\mathrm{sig}^{b_1}\bar{\boldsymbol{e}}_{\boldsymbol{\Omega}}-k_2\mathrm{sig}^{b_2}\bar{\boldsymbol{e}}_{\boldsymbol{\Omega}}-k_3\mathrm{sig}^{b_3}\boldsymbol{S}_{\boldsymbol{\Omega}}-\\&k_4\mathrm{sig}^{b_4}\boldsymbol{S}_{\boldsymbol{\Omega}}-k_5\tanh\frac{\boldsymbol{S}_{\boldsymbol{\Omega}}}{w}+\boldsymbol{u}_{\mathrm{comp}}\Big),\end{aligned} \quad (18)$$

where

$$\boldsymbol{u}_{\mathrm{comp}}=-k_{\boldsymbol{\Omega}}\mathrm{e}^{|\tanh(\dot{\boldsymbol{S}}_{\boldsymbol{\Omega}})|}\frac{\mathrm{d}\boldsymbol{S}_{\boldsymbol{\Omega}}(t)}{\mathrm{d}t}, \quad (19)$$

where the constant $k_{\boldsymbol{\Omega}}>0$, and the coefficient $\mathcal{K}_{\boldsymbol{\Omega}}=k_{\boldsymbol{\Omega}}\mathrm{e}^{|\tanh(\dot{\boldsymbol{S}}_{\boldsymbol{\Omega}})|}$ has a parameter range of $\mathcal{K}_{\boldsymbol{\Omega}}\in(k_{\boldsymbol{\Omega}},2.718k_{\boldsymbol{\Omega}})$. The term $\frac{\mathrm{d}\boldsymbol{S}_{\boldsymbol{\Omega}}(t)}{\mathrm{d}t}$ can initially be approximated by the following equation, and the explanation can be found in Eqs. (S16) and (S17) of the ESM.

$$\dot{\boldsymbol{S}}_{\boldsymbol{\Omega}}(t_0)=\frac{\mathrm{d}\boldsymbol{S}_{\boldsymbol{\Omega}}(t_0)}{\mathrm{d}t}\approx\frac{\boldsymbol{S}_{\boldsymbol{\Omega}}(t_0+h_{\mathrm{s}})-\boldsymbol{S}_{\boldsymbol{\Omega}}(t_0)}{h_{\mathrm{s}}}, \quad (20)$$

where h_{s} is the time step.

Lemma 5 Considering the designed virtual angle controller Eq. (18), the constructed sliding mode manifold $\boldsymbol{S}_{\boldsymbol{\Omega}}$ will be fixed-time stable with analytical settling time $T_{\boldsymbol{\Omega}}$. The detailed proof process can be found in Section S4 of the ESM.

For the attitude angular rate subsystem, the angular rate errors are denoted as $\boldsymbol{e}_{\boldsymbol{\omega}}=[e_q,\ e_r,\ e_p]^{\mathrm{T}}\in\mathbb{R}^3$. Similar to Eq. (16), the angular rate sliding mode manifold $\boldsymbol{S}_{\boldsymbol{\omega}}$ is given by

$$\boldsymbol{S}_{\boldsymbol{\omega}}=\boldsymbol{e}_{\boldsymbol{\omega}}+c_{\boldsymbol{\omega}}\int_0^t\boldsymbol{e}_{\boldsymbol{\omega}}\,\mathrm{d}\tau+\int_0^t l_1\,\mathrm{sig}^{c_1}\boldsymbol{e}_{\boldsymbol{\omega}}+l_2\mathrm{sig}^{c_2}\boldsymbol{e}_{\boldsymbol{\omega}}\mathrm{d}\tau, \quad (21)$$

where the coefficients $c_{\boldsymbol{\omega}}$, l_1, $l_2>0$, $c_1>1$, and $0<c_2<1$. The derivative of $\boldsymbol{S}_{\boldsymbol{\omega}}$ with respect to time t is

$$\dot{\boldsymbol{S}}_{\boldsymbol{\omega}}=\boldsymbol{f}_{\boldsymbol{\omega}}+\boldsymbol{g}_{\boldsymbol{\omega}}\boldsymbol{u}+\boldsymbol{\Delta}_{\boldsymbol{\omega}}+c_{\boldsymbol{\omega}}\boldsymbol{e}_{\boldsymbol{\omega}}+l_1\mathrm{sig}^{c_1}\boldsymbol{e}_{\boldsymbol{\omega}}+l_2\mathrm{sig}^{c_2}\boldsymbol{e}_{\boldsymbol{\omega}}. \quad (22)$$

Then, the designed actual control input $\boldsymbol{u}^*$ is given by

$$\begin{aligned}\boldsymbol{u}^*=\boldsymbol{g}_{\boldsymbol{\omega}}^{-1}\Big(&-\boldsymbol{f}_{\boldsymbol{\omega}}-\hat{\boldsymbol{\Delta}}_{\boldsymbol{\omega}}-c_{\boldsymbol{\omega}}\boldsymbol{e}_{\boldsymbol{\omega}}-l_1\mathrm{sig}^{c_1}\boldsymbol{e}_{\boldsymbol{\omega}}-\\&l_2\mathrm{sig}^{c_2}\boldsymbol{e}_{\boldsymbol{\omega}}-k_6\mathrm{sig}^{c_3}\boldsymbol{S}_{\boldsymbol{\omega}}-k_7\mathrm{sig}^{c_4}\boldsymbol{S}_{\boldsymbol{\omega}}-\\&k_8\tanh\frac{\boldsymbol{S}_{\boldsymbol{\omega}}}{w}-k_{\boldsymbol{\omega}}\mathrm{e}^{|\tanh(\dot{\boldsymbol{S}}_{\boldsymbol{\omega}})|}\dot{\boldsymbol{S}}_{\boldsymbol{\omega}}\Big),\end{aligned} \quad (23)$$

where k_6, k_7, k_8, $k_\omega>0$, $c_3>1$, $0<c_4<1$, and the coefficient $\mathcal{K}_\omega=k_\omega e^{|\tanh(\boldsymbol{S}_\omega)|}$ satisfies $\mathcal{K}_\omega\in(k_\omega,\ 2.718k_\omega)$.

Lemma 6 Considering the designed real controller Eq. (23), the constructed sliding mode manifold $\boldsymbol{S}_\omega$ will be fixed-time stable with analytical settling time T_ω. The detailed proof process is similar to that of Lemma 5 and can also be found in Section S4 of the ESM.

3.4 Integrated stability analysis and discussion

In summary, the sliding mode motion can be divided into two stages: (1) first, the sliding mode variables $\boldsymbol{S}_{\boldsymbol{\Omega}}$ and $\boldsymbol{S}_\omega$ converge to sliding mode hyperplanes ($\boldsymbol{S}_{\boldsymbol{\Omega}}\to 0$, $\boldsymbol{S}_\omega\to 0$) from arbitrary initial states of the system; (2) second, the system states reach the equilibrium points ($\boldsymbol{e}_{\boldsymbol{\Omega}}\to 0$, $\boldsymbol{e}_\omega\to 0$) along the hyperplanes. Having obtained the fixed-time convergence properties of the first stage from Lemmas 5 and 6, the stability analysis of the second stage is discussed in this section.

Theorem 2 Consider the transformed attitude error system Eq. (15), with the arbitrary initial conditions given. If the sliding mode surfaces $\boldsymbol{S}_{\boldsymbol{\Omega}}$ and $\boldsymbol{S}_\omega$ converge to the effective residual sets, then the proposed AFTR observer Eq. (8) with weight updating law $\hat{\boldsymbol{W}}$ and controllers (Eqs. (18) and (23)) with suitable parameters can guarantee that the observation errors $\tilde{\boldsymbol{\Delta}}_{\boldsymbol{\Omega}}$, $\tilde{\boldsymbol{\Delta}}_\omega$ and the state errors $\bar{\boldsymbol{e}}_{\boldsymbol{\Omega}}$, $\boldsymbol{e}_\omega$ can achieve a fast convergence to the equilibrium points in fixed time. Furthermore, the defined auxiliary state s_e can also converge to the original points, which means that the attitude angle error $\boldsymbol{e}_{\boldsymbol{\Omega}}$ will converge to the reference trajectory $\boldsymbol{e}_{\mathrm{op}}$ in the fixed time, i.e., the fixed-time tracking control results of actual attitude angles can be obtained. The complete proof process can be found in Section S5 of the ESM.

3.5 Parameter tuning guideline

Despite the relationship among some parameters, there is still a lack of guidance on how to fine-tune the main parameters so that the proposed observers and controllers can achieve the desired control performance. This section provides parameter-tuning tips for the AFTR, funnel boundaries, and fixed-time controllers. Meanwhile, the trade-off of convergence velocity and steady-state error range must be balanced simultaneously for the highly nonlinear system of high-speed aircraft. The control inputs are sensitive to a number of controller parameters from the funnel function depicted in Eq. (12) and the controllers illustrated in Eqs. (18) and (23), which may lead to the accumulation of errors and delays during the convergence process.

First, to enable the funnel boundary to guide error convergence behavior, an effective initial threshold ρ_0 needs to be provided, generally not less than the maximum initial state error. Then, a feasible parameter factor k_s is needed, which indicates the final steady-state error. A rapid convergence trajectory needs a large shrinking rate, which significantly adjusts the convergence speed of the prescribed performance boundary. The shrinking rate can be selected from the range $l\in[0.5, 3.0]$ in this paper. Furthermore, $\rho_{i,\infty}$ defines the final steady-state error boundary of angle state i, and the order of magnitude is less than 10^{-2} in this article. Except for the above crucial parameters, the convergence process of the state error is not sensitive to other PPC parameters.

Second, in the fixed-time controller, the exponents of the fixed-time convergence terms, denoted as b_1, b_2, b_3, b_4, c_1, c_2, c_3, and c_4, need to be determined appropriately according to Lemmas 1 and 2. Generally, b_1, b_3, c_1, $c_3>1$ and b_2, b_4, c_2, $c_4\in(0,\ 1)$. The parameters b_1, b_3, c_1, and c_3 need to be carefully selected, and the effective value is not greater than 5 in this article. After that, the control coefficients l_1, l_2, and k_j ($j=1, 2, \cdots, 8$) can be set to 1 and then modified according to the system's behavior. Regarding the second integral terms in sliding mode manifolds Eqs. (16) and (21), the coefficients k_1, k_2 and l_1, l_2 should be much smaller than the coefficients k_3, k_4, k_5, k_6, k_7, and k_8 in the main control terms. To reduce the effort needed to tune these control coefficients, similar terms can have the same coefficient settings between Eqs. (18) and (23) in the initial consideration. Furthermore, the coefficients $k_{\boldsymbol{\Omega}}$ and k_ω of the ancillary control terms should not be greater than 0.1.

With respect to the AFTR observer, the parameter design principle incorporates the following components:

(1) The numerical approximation capability of the neural network is directly influenced by the selection of m_j. Following the design principle of the Gaussian basis function, the approximation of input signals x_i can be enhanced by increasing the number of centroids of m_j and decreasing the Euclidean distance between m_j and x_i with nonlinear selection methods such as the Gaussian distribution.

(2) The variable n_j represents the bandwidth of the Gaussian basis function, which determines the mapping

capability of the NN to state inputs. Typically, the parameter should satisfy the range $n_j \geqslant 1$.

Remark 6 Table 1 systematically summarizes all generic parameters and their corresponding values used in the controllers presented in this study. It not only provides typical empirical ranges of these parameters (derived from a comprehensive review and synthesis of related literature), but also specifies the actual values adopted in the simulation cases in accordance with these recommended ranges. This clarifies the connection between parameter guidance ranges and the specific values chosen for numerical simulations.

4 Simulation verification

In this section, we describe the validation and comparative analysis of the proposed observer and controller. The first subsection focuses on the feasibility verification of the proposed attitude-integrated controller with the AFTR observer. The subsequent subsection evaluates control methods from the literature and highlights the reliability and robustness of the proposed framework.

The initial flight states of a winged-cone high-speed aircraft were given as $H=33.5$ km, $V=2590$ m/s, $\alpha=-2°$, $\beta=-1.5°$, and $\mu=-0.43°$, and the other initial states were all set to zero. The parameters associated with the different modules integrated in the attitude tracking control system are summarized in Table 1. Some matrix parameters were as follows: the initial weights of the RBFNN are given by $\boldsymbol{W}_0=\boldsymbol{0}_{N\times 1}$, and the coefficients are $\{C_1, C_2, \cdots, C_j, \cdots, C_N\}\in\{-0.05, -0.0498, \cdots, 0, \cdots, 0.05\}$. The following cases are discussed.

4.1 Nominal cases

Along with the designed parameters, three validation scenarios were executed in this subsection.

(1) Performance verification with the original PPC (Bechlioulis and Rovithakis, 2008) and the FGFTC

In this case, a comparative validation was performed to highlight the advantages of the proposed FGFTC. The tracking error results with the proposed performance guidance strategy are shown in Fig. 2, which compares the convergence trajectories in three-channel angle errors with different control factors k_s= 0.4, 0.5, 0.6. The results indicate that the angle errors can rapidly and accurately track the reference trajectories and achieve convergence without extra transition behaviors. Additionally, the overall convergence time of the angle subsystem is determined by the slowest convergence angle, and the close coupling among the three-channel parameters may delay the convergence speed.

The advantages and robustness of the proposed strategy compared to the traditional PPC of Bechlioulis and Rovithakis (2008) are illustrated in Fig. 3. The most apparent advantage is the tight steady-state error range and the superiority of the convergence speed, indicating that the angle errors can rapidly converge while remaining stable along with the reference error trajectories. We also conclude that the angle errors in FGFTC can reach 10^{-2} orders of magnitude, yet the original PPC method cannot achieve this target. Fig. 3 shows the maximum achievable convergence speed and minimum steady-state error range of the original PPC method. Obviously, there is a gap between the original PPC and the method presented in this article.

(2) Performance of AFTR

Some time-varying disturbances were introduced into the dynamic model, and then the performance of the designed AFTR was verified.

Table 1 Empirical range of parameter tuning

Module	Parameter	Empirical range	Simulation value
Funnel module	ρ_0, k_s, l, $\rho_{i,\inf}$, a_ρ	$\rho_0>e_0$; $k_s\in[0, 1]$; $l>0$; $\rho_{i,\inf}>0$; $a_\rho\in(0, 1)$	$\rho_0>e_{i,0}$; $i=\alpha, \beta, \mu$; $k_s=0.6$; $l\in[0.5, 3.0]$; $\rho_{i,\inf}=0.01$; $a_\rho=10^{-4}$
AFTR observer	$\mathcal{N}$, $\boldsymbol{P}$, a_1, $c_{1,i}$, $c_{2,i}$, d_n	$\mathcal{N}>0$; $a_1\in(0, 1)$; $c_{1,i}>0$;$c_{2,i}>0$; $d_n>1$; $p_{1,i}>0$; $p_{i,i}\in\boldsymbol{P}$	$\mathcal{N}=500$; $a_1=0.5$; $c_{1,i}=c_{2,i}=1$; $d_n=1.5$; $\boldsymbol{P}=\mathrm{diag}\{4, 4, 4, 1, 1, 1\}$
Angle tracking subsystem	c_0, b_1, b_2, k_1, k_2, b_3, b_4, k_3, k_4, k_5, w, $k_{\boldsymbol{\Omega}}$	$c_0>0$; $b_1, b_3>1$; $0<b_2, b_4<1$; $w>0$; $k_1, k_2, k_3, k_4, k_5>0$; $k_{\boldsymbol{\Omega}}>0$	$0<k_{\boldsymbol{\Omega}}<0.1$; $c_0=0.02$; $b_1=1.5$; $b_2=0.6$; $b_3=5.0$; $b_4=0.8$; $k_1=2\times10^{-5}$; $k_2=3\times10^{-5}$; $k_3=0.5$; $k_4=0.001$; $k_5=0.03$; $w=1$
Angular rate tracking subsystem	c_ω, l_1, l_2, c_1, c_2, k_6, k_7, k_8,c_3, c_4, k_ω	$c_\omega>0$; $c_1, c_3>1$; $0<l_1, l_2<1$; $0<c_2, c_4<1$; $k_6, k_7, k_8>0$; $k_\omega>0$	$0<k_\omega<0.1$; $c_\omega=3$; $l_1=2\times10^{-5}$; $l_2=3\times10^{-5}$; $c_1=1.6$; $c_2=0.8$; $c_3=2$; $c_4=0.2$; $k_6=3$; $k_7=0.015$; $k_8=0.03$

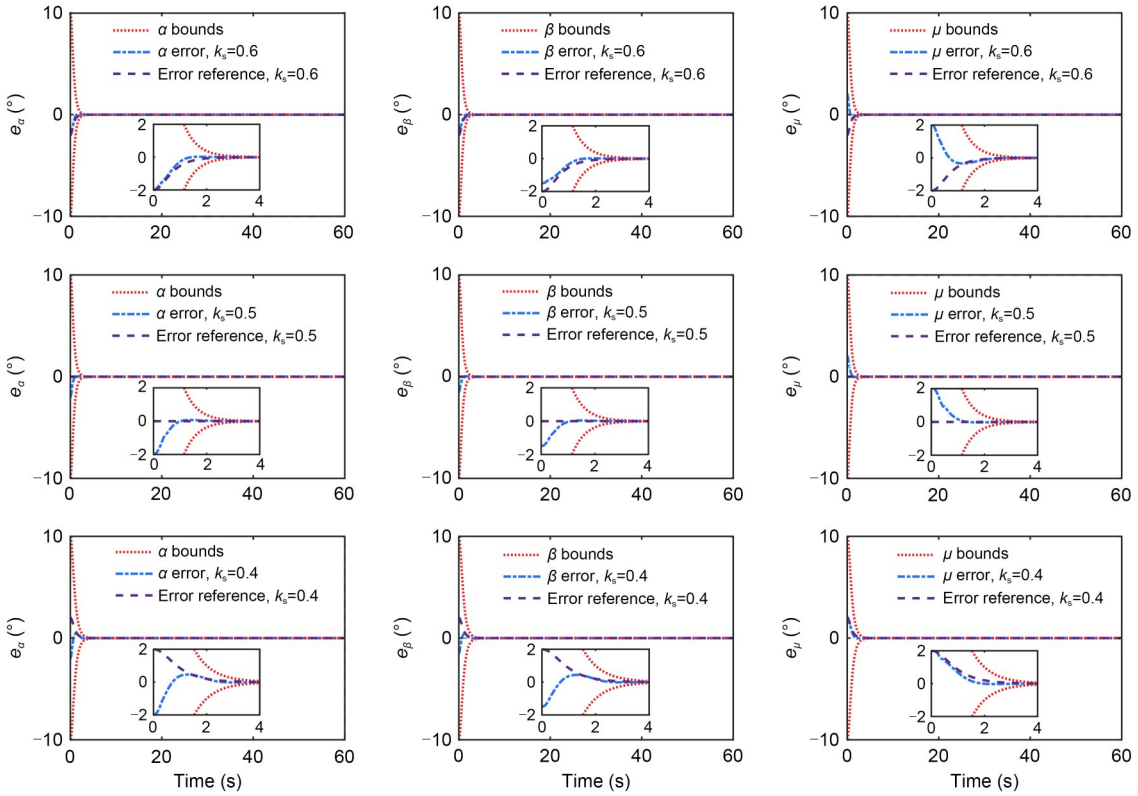

Fig. 2 Error convergence trajectories of attitude angles following the reference trajectories obtained under different control coefficients k_s

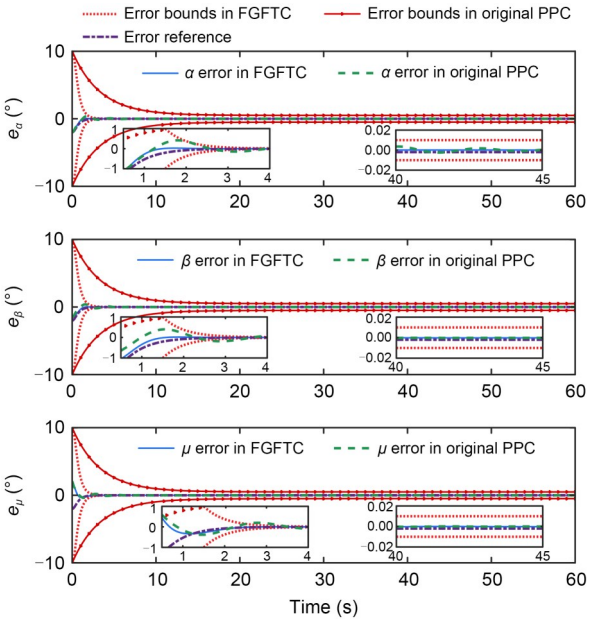

Fig. 3 Tracking errors and bounds of attitude angles compared with original PPC methods

$$\Delta_{\Omega}=(0.02\sin(5\pi t)+0.03\cos(2\pi t))\cdot[1,\ 1,\ 1]^{\mathrm{T}}, \quad (24)$$

$$\Delta_{\omega}=(0.02\sin(10\pi t)+0.03\cos(5\pi t))\cdot[1,\ 1,\ 1]^{\mathrm{T}}. \quad (25)$$

The above disturbance expressions consider that the angular rates may experience perturbation effects at a greater frequency than angle variables. Figs. 4 and 5 show that the external unmatched disturbances within the attitude angle channel and angular rate channel are well estimated by the proposed AFTR observer. The approximation errors of the attitude angle in the three channels shown in Fig. 4 have a maximum of [2.5264°, 1.2720°, 2.3290°] and an average error of [0.0568°, 0.0432°, 0.0667°], which meets the required estimation accuracy throughout the total flight process. Meanwhile, the approximation errors of the attitude angular rates in the three channels in Fig. 5 are [13.7805 (°)/s, 7.6778 (°)/s, 25.8006 (°)/s] at maximum in the transition time node and [0.4149 (°)/s, 0.1656 (°)/s, 0.1639 (°)/s] on average during the stable convergence process. The fluctuations with deviation occur within the first 15 s, which may be caused by additional unknown uncertainties produced by the propagation of estimated errors from the outer-loop to the inner-loop channel. Eventually, these deviations will be eliminated under fixed-time compensation control.

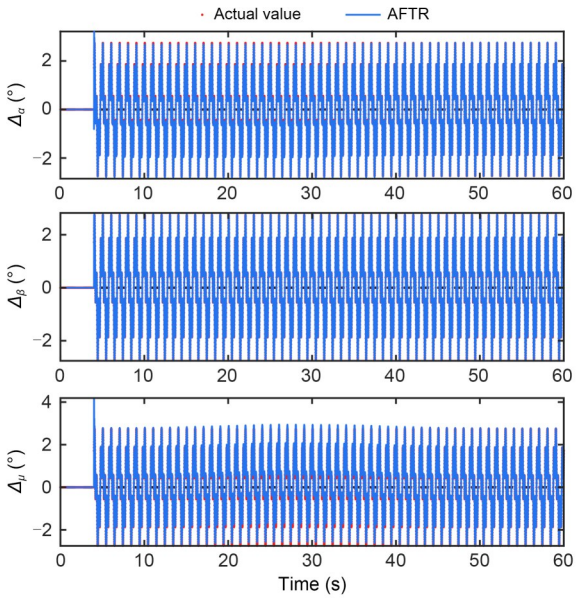

Fig. 4 Disturbance approximation in the attitude angle channel

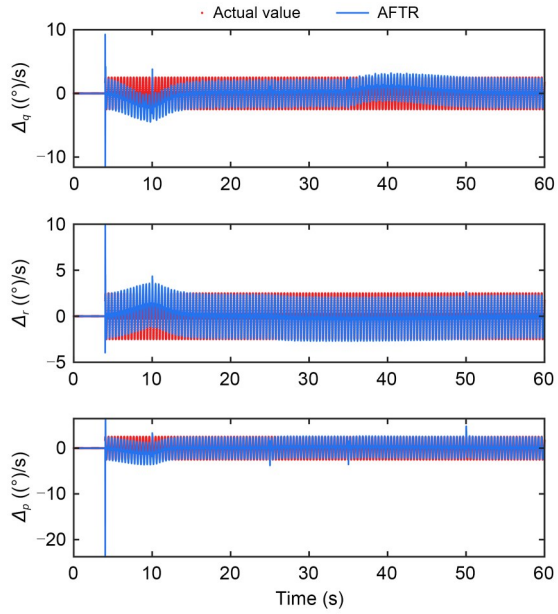

Fig. 5 Disturbance approximation in the angular rate channel

(3) Integrated performance verification with disturbances and uncertainties

Taking model uncertainties, aerodynamic and atmospheric parameters, external disturbances from Eqs. (24) and (25), and other perturbation factors into account, Figs. 6 and 7 show that the steady-state errors for both angle and angular rates are all less than 10^{-2} magnitude with the compensation control of AFTR,

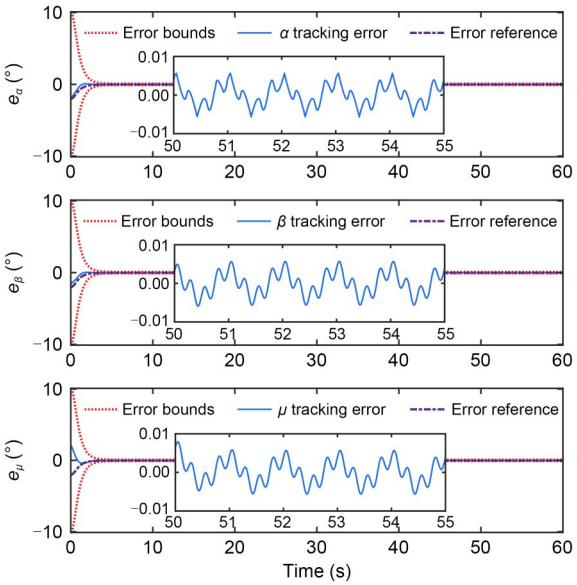

Fig. 6 Tracking errors of the angle with the observer

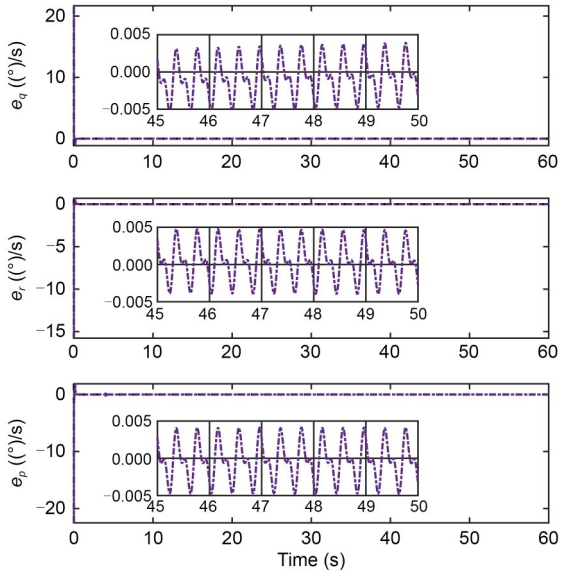

Fig. 7 Tracking errors of the angular rate with the observer

which is interrelated to the performance verification in Fig. 3.

The control inputs in Fig. 8 can rapidly respond to and correct the introduced disturbances and uncertainties, and the sudden change in curves is first reflected in Fig. 5. The reason for this phenomenon is the short-lived intense response of the control system to sudden perturbations. The designed sliding mode manifolds in the three channels can achieve effective convergence in a fixed time (Fig. 8). Consistency between the convergence trends of the angle sliding mode manifolds

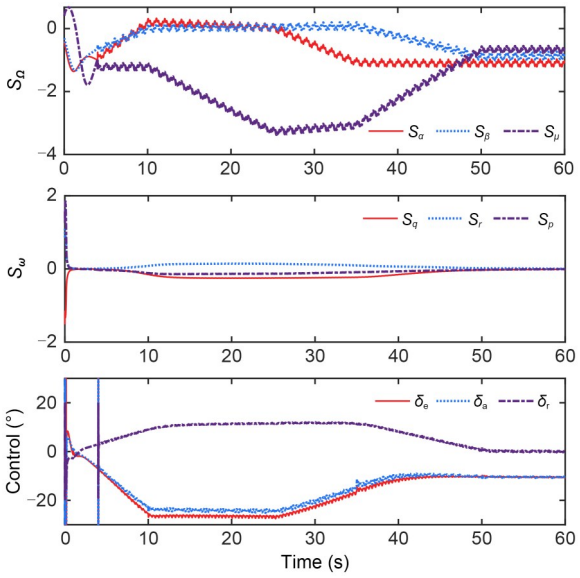

Fig. 8 Sliding mode manifolds and control inputs with an observer. δ_e, δ_a, and δ_r represent the left elevator, right elevator, and rudder, respectively

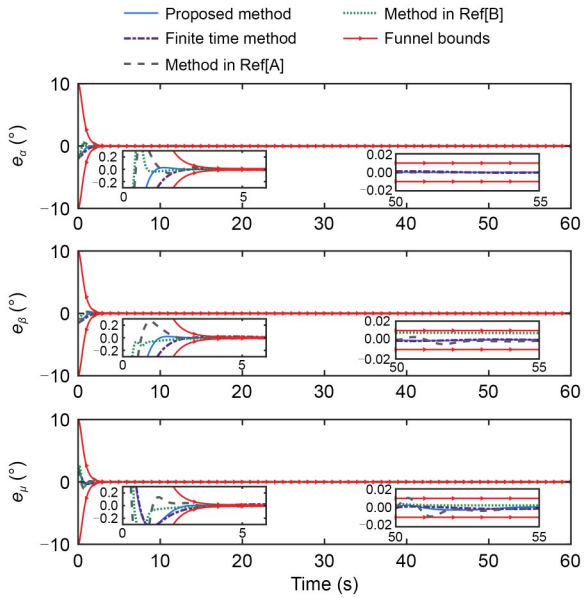

Fig. 9 Tracking errors and bounds of attitude angles of the proposed method compared with those of another three methods

and the reference angle signals can be obtained when introducing the continuous smooth reference angle signals and effective controller. The above discussion shows that the designed observer and controller can achieve robust control of a complex attitude system for high-speed aircraft.

4.2 Comparative case

Excluding the effects of external disturbances while keeping the parameter uncertainties, in this section, we describe a comparative analysis among the proposed controller, the finite-time controller, the fuzzy fixed-time sliding mode controller of Chen et al. (2023) denoted as Ref[A], and the proportional-integral (PI) controller of Bu et al. (2023) denoted as Ref[B]. The comparative results are shown in Figs. 9–15. The angle error profiles in Fig. 9 and actual angle tracking profiles in Fig. 10 show that the proposed controller can achieve more precise convergence than the other three methods, characterized by the absence of overshooting and severe oscillations. Similarly, the tracking errors of angular rates in Fig. 11 and the actual signal tracking trajectories in Fig. 12 show stable and excellent results under the funnel-guided fixed-time sliding mode scheme. Defining the average control energy as $E_i = 0.5\left(\sum_{t=0}^{60} u_i(t)/60\right)^2$, $i=1, 2, 3$, where i represents the angle channel and u_i is the actual control input, from

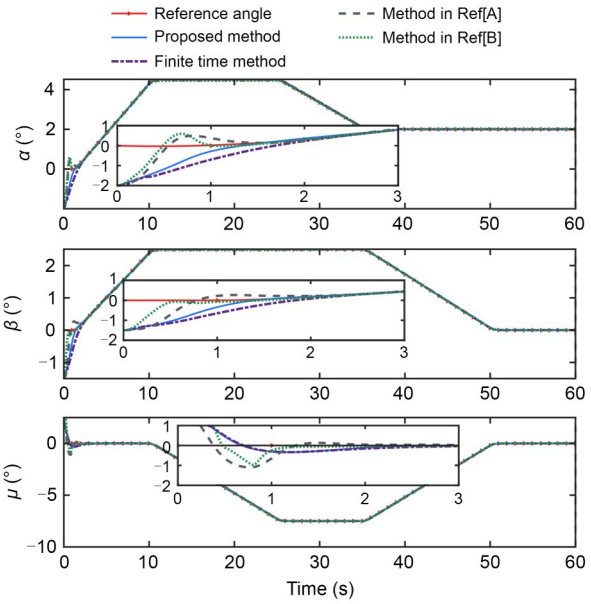

Fig. 10 Tracking trajectories of attitude angles of the proposed method compared to those of another three methods

radar figures presented in Figs. 13–15, the control performance of the proposed method in the three channels was better than that of the other three methods with respect to settling time, steady-state accuracy, and average control energy, which intuitively reflect faster error convergence and higher tracking accuracy with less energy loss.

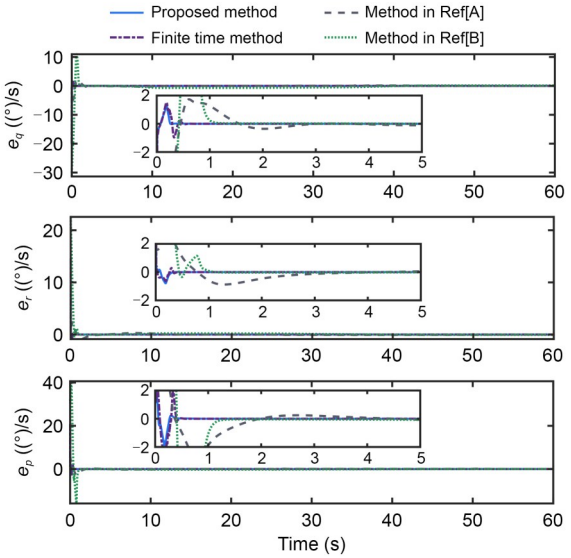

Fig. 11 Tracking errors and bounds of angular rates of the proposed method compared with those of another three methods

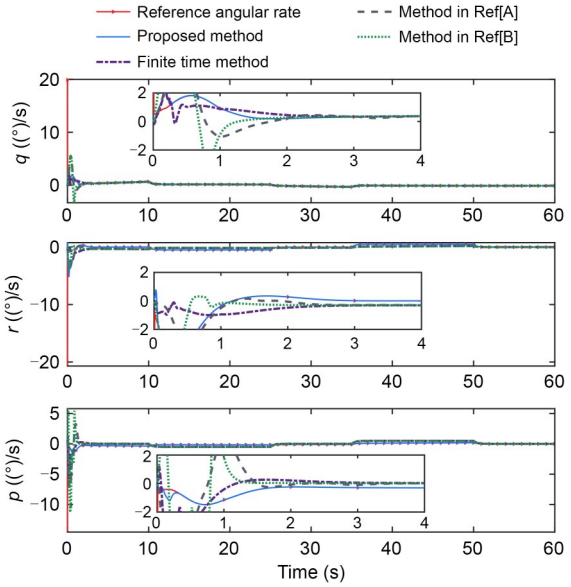

Fig. 12 Tracking trajectories of angular rates of the proposed method compared with those of another three methods

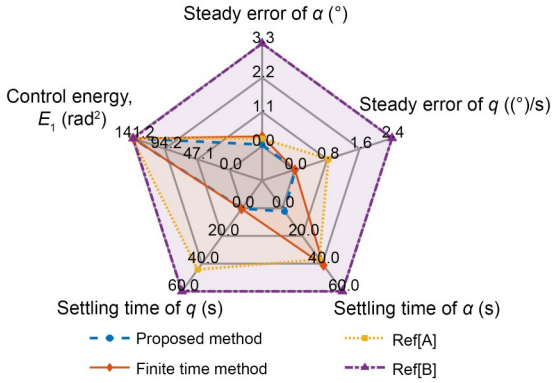

Fig. 13 Radar figure comparing the control performance of α and q in the pitch channel, including the total control energy, steady-state error, and settling time

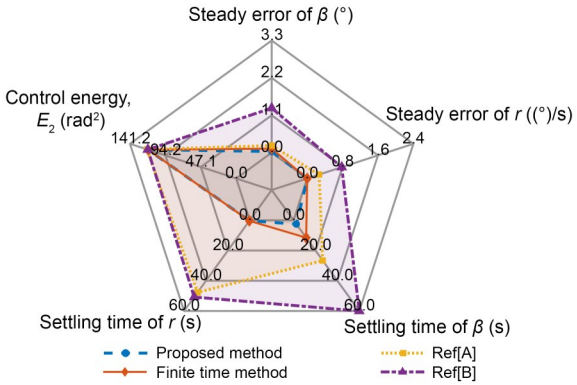

Fig. 14 Radar figure comparing the control performance of β and r in the yaw channel, including the total control energy, steady-state error, and settling time

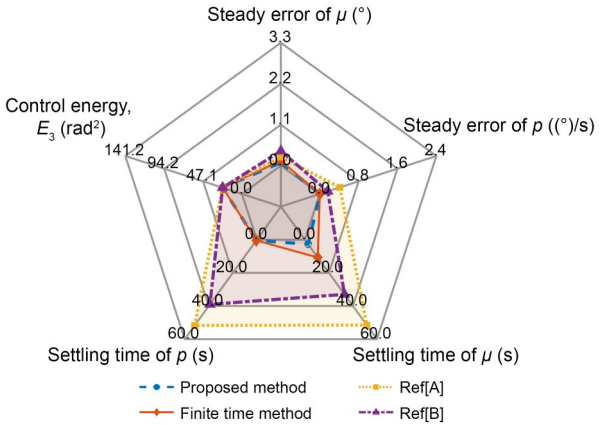

Fig. 15 Radar figure comparing the control performance of μ and p in the roll channel, including the total control energy, steady-state error, and settling time

5 Conclusions

In this article, we presented a funnel-guided performance-prescribed fixed-time robust attitude control framework with an AFTR observer for high-speed aircraft. An adaptive parameter-updating AFTR observer was first constructed based on second-order error dynamics to perceive the control system's real-time variation. Then, we considered an effective funnel function and error convergence strategy for controllable

transition and steady-state performance. To ensure the robustness and rapidity of the entire closed-loop flight control system, we propose a double-integral fixed-time sliding mode control scheme and an oscillation-suppression skill by a designed auxiliary function during the convergence stage. The resulting simulation findings suggest that the control performance desired for high-speed aircraft can be achieved in the presence of unknown uncertainties. Overall, the composite control scheme proposed in this paper can accomplish attitude control tasks for high-speed aircraft under strong nonlinearity and complex coupling with remarkable steady-state error and a robust convergence process. Based on the similarities in system modeling approaches and the empirical guidelines for parameter fine-tuning, the proposed composite controller can also be effectively applied to tracking control tasks in other nonlinear systems.

Acknowledgments

This work is supported by the National Natural Science Foundation of China (No. 11972368) and the Natural Science Foundation of Hunan Province (No. 2021JJ10045), China.

Author contributions

Kai AN designed the research, processed the corresponding data, and wrote the first draft of the manuscript. Wei HUANG and Shuangxi LIU helped to organize the manuscript. Kai AN and Wei HUANG revised and edited the final version.

Conflict of interest

Kai AN, Wei HUANG, and Shuangxi LIU declare that they have no conflict of interest.

References

An K, Guo ZY, Huang W, et al., 2022. Leap trajectory tracking control based on sliding mode theory for hypersonic gliding vehicle. *Journal of Zhejiang University-SCIENCE A*, 23(3):188-207. https://doi.org/10.1631/jzus.A2100362

Bao CY, Wang P, Tang GJ, 2023. Data-driven based model-free adaptive optimal control method for hypersonic morphing vehicle. *IEEE Transactions on Aerospace and Electronic Systems*, 59(4):3713-3725. https://doi.org/10.1109/TAES.2022.3230633

Bechlioulis CP, Rovithakis GA, 2008. Robust adaptive control of feedback linearizable MIMO nonlinear systems with prescribed performance. *IEEE Transactions on Automatic Control*, 53(9):2090-2099. https://doi.org/10.1109/TAC.2008.929402

Berger T, Rauert AL, 2020. Funnel cruise control. *Automatica*, 119:109061. https://doi.org/10.1016/j.automatica.2020.109061

Bouaiss O, Mechgoug R, Taleb-Ahmed A, et al., 2024. Robust trajectory tracking of quadrotors using adaptive radial basis function network compensation control. *Journal of the Franklin Institute*, 361(3):1167-1185. https://doi.org/10.1016/j.jfranklin.2023.12.045

Bu XW, 2023. Prescribed performance control approaches, applications and challenges: a comprehensive survey. *Asian Journal of Control*, 25(1):241-261. https://doi.org/10.1002/asjc.2765

Bu XW, Xiao Y, 2018. Prescribed performance-based low-computational cost fuzzy control of a hypersonic vehicle using non-affine models. *Advances in Mechanical Engineering*, 10(2):1-12. https://doi.org/10.1177/1687814018757261

Bu XW, Hua CC, Lv ML, et al., 2023. Flight control of waverider vehicles with fragility-avoidance prescribed performance. *IEEE Transactions on Aerospace and Electronic Systems*, 59(5):5248-5261. https://doi.org/10.1109/TAES.2023.3251314

Chen HL, Wang P, Tang GJ, 2023. Fuzzy disturbance observer-based fixed-time sliding mode control for hypersonic morphing vehicles with uncertainties. *IEEE Transactions on Aerospace and Electronic Systems*, 59(4):3521-3530. https://doi.org/10.1109/TAES.2022.3227886

Chen LL, Liu ZB, Dang QQ, et al., 2024. Robust fixed-time flight controller for a dual-system convertible UAV in the cruise mode. *Defence Technology*, 39:53-66. https://doi.org/10.1016/j.dt.2024.04.009

Chen M, Wang HQ, Liu XP, 2021. Adaptive fuzzy practical fixed-time tracking control of nonlinear systems. *IEEE Transactions on Fuzzy Systems*, 29(3):664-673. https://doi.org/10.1109/TFUZZ.2019.2959972

Ding YB, Yue XK, Liu C, et al., 2022. Finite-time controller design with adaptive fixed-time anti-saturation compensator for hypersonic vehicle. *ISA Transactions*, 122:96-113. https://doi.org/10.1016/j.isatra.2021.04.038

Dong ZH, Li YH, Lv ML, et al., 2022. Fuzzy adaptive prescribed performance fault-tolerant control for HFVs with fixed-time convergence guarantee. *International Journal of Aerospace Engineering*, 2022:2438657. https://doi.org/10.1155/2022/2438657

Guo YY, Xu B, 2022. Finite-time deterministic learning command filtered control for hypersonic flight vehicle. *IEEE Transactions on Aerospace and Electronic Systems*, 58(5):4214-4225. https://doi.org/10.1109/TAES.2022.3160687

Keshmiri S, Mirmirani M, Colgren R, 2012. Six-DOF modeling and simulation of a generic hypersonic vehicle for conceptual design studies. AIAA Modeling and Simulation Technologies Conference and Exhibit, p.1-12. https://doi.org/10.2514/6.2004-4805

Li CY, Wang W, Liu ZJ, et al., 2024. Adaptive neural network based fixed-time attitude tracking control of spacecraft

considering input saturation. *Aerospace Science and Technology*, 155:109746. https://doi.org/10.1016/j.ast.2024.109746

Li WT, Zhao JS, Su SW, et al., 2023. Adaptive output feedback attitude control for reusable launch vehicle with input constraints and actuator faults. *Aerospace Science and Technology*, 142:108616. https://doi.org/10.1016/j.ast.2023.108616

Liu SH, Yan JG, Cao JF, et al., 2021. Review of the precise orbit determination for Chinese lunar exploration projects. *Earth and Space Science*, 8(4):e2020EA001361. https://doi.org/10.1029/2020EA001361

Lun YB, Wang HL, Wu TC, et al., 2024. A changeable boundary prescribed performance control for the altitude ground test facility. *Nonlinear Dynamics*, 112(6):4483-4506. https://doi.org/10.1007/s11071-023-09270-4

Meng Y, Yu X, Zhu YK, et al., 2024. Fixed-time attitude control of reusable launch vehicles utilizing reliability-based control allocation. *Control Engineering Practice*, 151:106013. https://doi.org/10.1016/j.conengprac.2024.106013

Moulay E, Léchappé V, Bernuau E, et al., 2022. Fixed-time sliding mode control with mismatched disturbances. *Automatica*, 136:110009. https://doi.org/10.1016/j.automatica.2021.110009

Parsegov S, Polyakov A, Shcherbakov P, 2012. Nonlinear fixed-time control protocol for uniform allocation of agents on a segment. The 51st IEEE Conference on Decision and Control, p.7732-7737. https://doi.org/10.1109/CDC.2012.6426570

Polyakov A, 2012. Nonlinear feedback design for fixed-time stabilization of linear control systems. *IEEE Transactions on Automatic Control*, 57(8):2106-2110. https://doi.org/10.1109/TAC.2011.2179869

Qian CJ, Lin W, 2001. Non-Lipschitz continuous stabilizers for nonlinear systems with uncontrollable unstable linearization. *Systems & Control Letters*, 42(3):185-200. https://doi.org/10.1016/S0167-6911(00)00089-X

Shen YX, Zhou DJ, Wu YD, et al., 2023. Anti-disturbance control for HVs system subject to nonlinear actuator characteristics with extended state observer. *Journal of the Franklin Institute*, 360(18):14676-14695. https://doi.org/10.1016/j.jfranklin.2023.10.005

Song JG, Zhang JX, 2024. Fault-tolerant prescribed performance control of nonlinear systems with process faults and actuator failures. *ISA Transactions*, 144:220-227. https://doi.org/10.1016/j.isatra.2023.11.010

Sun JL, Yi JQ, Pu ZQ, et al., 2020. Fixed-time sliding mode disturbance observer-based nonsmooth backstepping control for hypersonic vehicles. *IEEE Transactions on Systems, Man, and Cybernetics: Systems*, 50(11):4377-4386. https://doi.org/10.1109/TSMC.2018.2847706

Tan J, Guo SJ, 2022. Backstepping control with fixed-time prescribed performance for fixed wing UAV under model uncertainties and external disturbances. *International Journal of Control*, 95(4):934-951. https://doi.org/10.1080/00207179.2020.1831700

Wang F, Zhou C, Hua CC, 2024. Adaptive predefined time neural filtered control design for an uncertain nonlinear system and application to flight control. *Applied Mathematical Modelling*, 129:25-47. https://doi.org/10.1016/j.apm.2024.01.044

Wang G, Xia HW, 2024. Fault-tolerant learning control of air-breathing hypersonic vehicles with uncertain parameters and actuator faults. *Expert Systems with Applications*, 238:121874. https://doi.org/10.1016/j.eswa.2023.121874

Wang YY, Hu JB, 2018. Improved prescribed performance control for air-breathing hypersonic vehicles with unknown deadzone input nonlinearity. *ISA Transactions*, 79:95-107. https://doi.org/10.1016/j.isatra.2018.05.008

Wu TC, Wang HL, Yu Y, et al., 2021. Quantized fixed-time fault-tolerant attitude control for hypersonic reentry vehicles. *Applied Mathematical Modelling*, 98:143-160. https://doi.org/10.1016/j.apm.2021.04.033

Wu YJ, Shao KJ, Wang N, et al., 2023. Finite-time path following control of a sailboat with actuator failure and unknown sideslip angle. *Journal of Zhejiang University-SCIENCE A*, 24(9):749-761. https://doi.org/10.1631/jzus.A2300184

Xin B, Cheng S, Wang Q, et al., 2023. Fixed-time prescribed performance consensus control for multiagent systems with non-affine faults. *IEEE Transactions on Fuzzy Systems*, 31(10):3433-3446. https://doi.org/10.1109/TFUZZ.2023.3255889

Xu SH, Guan YZ, Wei CZ, et al., 2022. Reinforcement-learning-based tracking control with fixed-time prescribed performance for reusable launch vehicle under input constraints. *Applied Sciences*, 12(15):7436. https://doi.org/10.3390/app12157436

Yin ZY, Wang B, Xiong RT, et al., 2024. Attitude tracking control of hypersonic vehicle based on an improved prescribed performance dynamic surface control. *The Aeronautical Journal*, 128(1323):875-895. https://doi.org/10.1017/aer.2023.79

Zhang BC, Liang YY, Rao ST, et al., 2024. RBFNN-based anti-input saturation control for hypersonic vehicles. *Aerospace*, 11(2):108. https://doi.org/10.3390/aerospace11020108

Zhang H, Wang P, Tang GJ, et al., 2023. Fixed-time sliding mode control for hypersonic morphing vehicles via event-triggering mechanism. *Aerospace Science and Technology*, 140:108458. https://doi.org/10.1016/j.ast.2023.108458

Zhang H, Wang P, Tang G, et al., 2024. Disturbance observer-based fixed-time control for hypersonic morphing vehicles with uncertainties. *The Aeronautical Journal*, 128(1326):1844-1874. https://doi.org/10.1017/aer.2023.116

Zhao HW, Yang LB, 2022. Global adaptive neural backstepping control of a flexible hypersonic vehicle with disturbance

estimation. *Aircraft Engineering and Aerospace Technology: An International Journal*, 94(4):492-504. https://doi.org/10.1108/AEAT-08-2020-0178

Zhao JQ, Feng DZ, Cui JS, et al., 2022. Finite-time extended state observer-based fixed-time attitude control for hypersonic vehicles. *Mathematics*, 10(17):3162. https://doi.org/10.3390/math10173162

Zhao SW, Wang JC, Xu HT, et al., 2023a. ADP-based attitude-tracking control with prescribed performance for hypersonic vehicles. *IEEE Transactions on Aerospace and Electronic Systems*, 59(5):6419-6431. https://doi.org/10.1109/TAES.2023.3276729

Zhao SW, Wang JC, Xu HT, et al., 2023b. Composite observer-based optimal attitude-tracking control with reinforcement learning for hypersonic vehicles. *IEEE Transactions on Cybernetics*, 53(2):913-926. https://doi.org/10.1109/TCYB.2022.3192871

Zuo ZY, 2015. Nonsingular fixed-time consensus tracking for second-order multi-agent networks. *Automatica*, 54:305-309. https://doi.org/10.1016/j.automatica.2015.01.021

Zuo ZY, Tie L, 2014. A new class of finite-time nonlinear consensus protocols for multi-agent systems. *International Journal of Control*, 87(2):363-370. https://doi.org/10.1080/00207179.2013.834484

Electronic supplementary materials

Sections S1–S5, Eqs. (S1)–(S38)